BIOCHEMISTRY
including biophysical chemistry & molecular biology
Article

Biochemistry **2010,** *49,* 195–206
DOI: 10.1021/bi901614m

Kinetic and Structural Characterization of Dihydrofolate Reductase from *Streptococcus pneumoniae*[†]

Jeeyeon Lee,[‡,∥] Neela H. Yennawar,[§,∥] Jongsik Gam,[‡] and Stephen J. Benkovic*[,‡]

[‡]*Department of Chemistry, 414 Wartik Laboratory, The Pennsylvania State University, University Park, Pennsylvania 16802 and* [§]*Huck Institutes of the Life Sciences, 8B Althouse Lab, The Pennsylvania State University, University Park, Pennsylvania 16802.* [∥]*These authors contributed equally to this work.*

Received September 15, 2009; Revised Manuscript Received November 25, 2009

ABSTRACT: Drug resistance associated with dihydrofolate reductase (DHFR) has emerged as a critical issue in the treatment of bacterial infections. In our efforts to understand the mechanism of a drug-resistant dihydrofolate reductase (DHFR) from a pathogenic bacterial source, we report the first kinetic characterization of *Streptococcus pneumoniae* DHFR (spDHFR) along with its X-ray structure. This study revealed that the kinetic properties of spDHFR were significantly different from those of *Escherichia coli* DHFR. The product (tetrahydrofolate) dissociation step that is the rate-limiting step in *E. coli* DHFR is significantly accelerated in spDHFR so that hydride transfer or a preceding step is rate-limiting. Comparison of the binding parameters of this enzyme to those of a mutant spDHFR (Sp9) confirmed that the Leu100 residue in spDHFR is the critical element for the trimethoprim (TMP) resistance. Steady-state kinetics exhibited a pH dependence in k_{cat}, which prompted us to elucidate the role of the new catalytic residue (His33) in the active site of spDHFR. Structural data of the Sp9 mutant in complex with NADPH and methotrexate confirmed the participation of His33 in a hydrogen bonding network involving a water molecule, the hydroxyl group of Thr119, and the carboxylate ion of Glu30. Sequence analysis of the DHFR superfamily revealed that the His residue is the major amino acid component at this position and is found mostly in pathogenic bacterial DHFRs. A mutation of Val100 to Leu demonstrated a steric clash of the leucine side chain with the side chains of Ile8 and Phe34, rationalizing weaker binding of trimethoprim to Leu100 DHFR. Understanding the role of specific amino acids in the active site coupled with detailed structural analysis will inform us on how to better design inhibitors targeting drug-resistant pathogenic bacterial DHFRs.

Streptococcus pneumoniae is one of the clinically important Gram-positive bacterial pathogens (*1*, *2*). The emergence of multidrug-resistant (MDR) *S. pneumoniae* strains has become a global concern (*3*). Resistance to trimethoprim/sulfamethoxazole (T/S) arises from mutations in the target enzyme dihydrofolate reductase (DHFR),[1] whose activity is necessary for the maintenance of the cellular level of tetrahydrofolate that is essential for the biosynthesis of purines, some amino acids, and thymidine. Therefore, DHFR has long been a target for the discovery of novel antibacterial agents as well as anticancer drugs (*4*−*8*). Previous structural studies have demonstrated a high level of structural homology and a similarity in catalytic properties among human, parasitic, and bacterial DHFRs in spite of the low levels of sequence identity (*9*). To exploit the slight structural, sequence, and activity differences between family members for inhibitor design, we determined the structure and turnover cycle for the *S. pneumoniae* DHFR (spDHFR) enzyme.

Trimethoprim (TMP), 5-substituted 2,4-diaminopyrimidine, is a selective inhibitor for bacterial DHFRs and has been widely used because of its broad spectrum of activity. Bacterial DHFRs bind TMP 2500-fold more tightly (200 nM) than human DHFR (0.08 nM) (*9*). However, because of the higher mutational rates of bacterial DHFRs, a large number of *S. pneumoniae* variants no longer bind the drug effectively as a consequence of mutations in the chromosomal DHFR gene (*2*). In general, TMP-resistant clinical isolates have multiple mutations in spDHFR, but a single mutation at position 100 (I100L) has been implicated as a main contributor to drug resistance (*10*, *11*). Our investigation of the kinetics and structure of spDHFR has provided valuable insights into the function of this position.

We present detailed pre-steady- and steady-state kinetic studies of spDHFR that have revealed the kinetic characteristics of this enzyme are significantly different from those of *Escherichia coli* DHFR (*12*) and in turn prompted us to explore the X-ray structure of spDHFR in detail. We were able to crystallize the wild-type enzyme as well as one mutant of DHFR with nine amino acids that differ from those in the wild-type spDHFR sequence [Sp9 (Figure 1A)]. The sequence of spDHFR aligned with *E. coli* and human DHFR is shown in Figure 1B. The level of sequence homology to those sequences is 35 and 26%, respectively. A comparison of the turnover kinetics and drug resistance of the two spDHFRs provides valuable information for improvements in drug design.

[†]This work was supported by National Institutes of Health Grant 1S10RR023439-01 to N.H.Y. This project is funded, in part, by a grant from the Pennsylvania Department of Health using Tobacco Settlement Funds.

*To whom correspondence should be addressed. E-mail: sjb1@psu.edu. Phone: (814) 865-2882. Fax: (814) 865-2973.

[1]Abbreviations: DHFR, dihydrofolate reductase; sp, *Streptococcus pneumoniae*; TMP, trimethoprim; MTX, methotrexate; NADPH, nicotinamide adenine dinucleotide phosphate (reduced form); H_2F, 7,8-dihydrofolate; H_4F, tetrahydrofolate; DDF, dideazatetrahydrofolate; PDB, Protein Data Bank; rmsd, root-mean-square deviation.

A)

```
S.pneumoniae      MTKKIVAIWAQDEEGVIGKDNRLPWHLPAELQHFKETTLNHAILMGRVTFDGMGRRLLPQ 60
Sp9               MTKKIVAIWAQDEEGVIGKDNRLPWYLPAELQHFKETTLNHAILMGRVTFDGMGRRLLPK 60
                  *************************:*********************************:

S.pneumoniae      RETLILTRNPEEKIDGAVTFQDVQSVLDWYQAQEKNLYILGGKQIFQAFEPYLDEVIVTH 120
Sp9               RETLILTRNPEEKIDGVATFHDVQSVLDWYSAQEKNLYIVGGKQIFQAFEPYLDEVIVTH 120
                  ****************..**:*********.********:********************

S.pneumoniae      IHARVEGDTYFPEEFDLSLFETVSSKFYAKDEKNPYDFTIQYRKRKEV 168
Sp9               IHARVEGDTYFPAEFDLSLFETVSSKFYTKDEKNPYDFTIQYRKRKEV 168
                  ************ ***************:*******************
```

B)

```
spDHFR          MTKKIVAIWAQDEEGVIGKDNRLPWH-LPAELQHFKETTLN-------HAILMGRVTFDG 52
ecDHFR          ---MISLIAALAVDRVIGMENAMPWN-LPADLAWFKRNTLD-------KPVIMGRHTWES 49
hDHFR           -VGSLNCIVAVSQNMGIGKNGDLPWPPLRNEFRYFQRMTTTSSVEGKQNLVIMGKKTWFS 59
                    :  * *   :  ** :. :**  *  ::  *:. *         : ::**: *: .

spDHFR          MGR--RLLPQRETLILTRNPEEKIDGAVTFQDVQSVLDWYQAQ------EKNLYILGGKQ 104
ecDHFR          IG---RPLPGRKNIILSSQPG--TDDRVTWVKSVDEAIAACGD------VPEIMVIGGGR 98
hDHFR           IPEKNRPLKGRINLVLSRELKEPPQGAHFLSRSLDDALKLTEQPELANKVDMVWIVGGSS 119
                :    * *  * .::*: :     :.        .       :         : ::**

spDHFR          IFQAFE--PYLDEVIVTHIHARVEGDTYFPEEFDLSLFETVSS---KFYAKDEKNPYDFT 159
ecDHFR          VYEQFL--PKAQKLYLTHIDAEVEGDTHFP-DYEPDDWESVFS---EFHDADAQNSHSYC 152
hDHFR           VYKEAMNHPGHLKLFVTRIMQDFESDTFFP-EIDLEKYKLLPEYPGVLSDVQEEKGIKYK 178
                :::     *   :: :*:*   .*.**.** : : . :: : .    :   : ::  .:

spDHFR          IQYRKRKEV 168
ecDHFR          FEILERR-- 159
hDHFR           FEVYEKND- 186
                ::  ::.
```

C)

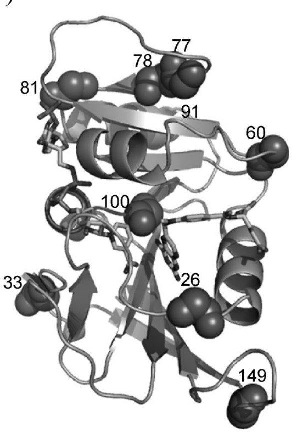

FIGURE 1: (A) Sequence of spDHFR and the mutant Sp9. Note that the Sp9 mutant DHFR has Val100 whereas the wild-type *S. pneumoniae* DHFR has Leu at this position. A list of nine mutations from *S. pneumoniae* DHFR includes H26Y, Q60K, A77V, V78A, Q81H, Q91S, L100V, E133A, and A149T. (B) Sequence alignment of DHFRs from *S. pneumoniae* (spDHFR), *E. coli* (ecDHFR), and human (hDHFR). The alignment was generated using the ClustalW2 web server (http://www.ebi.ac.uk/Tools/clustalw2/index.html). (C) Locations of the nine mutations in Sp9 DHFR. Note that most of these mutations are on the surface of the protein except the L100V mutation.

MATERIALS AND METHODS

Plasmid and Construction of Mutant Proteins. The plasmids containing the Sp9 DHFR mutant as well as wild-type spDHFR were kind gifts from R. Ranganathan at the University of Texas Southwestern Medical Center (Dallas, TX). The locations of the nine mutations in Sp9 are presented in Figure 1C. Site-directed mutagenesis was conducted for the creation of the His33Phe spDHFR mutant as described in the protocol provided in the Stratagene instruction manual.

Protein Expression and Purification. *E. coli* strain ER2566 (from NEB, IMPACT System) was modified to have a deletion of the DHFR gene (*folA*) and thymidylate synthethase (*thyA*) based on the protocol described in ref *13* and was used for the expression of the DHFR proteins. *E. coli* ER2566 Δ*thy*Δ*fol* cells containing the DHFR genes in a pET28a vector were grown at 37 °C to midlog phase in 500 mL of LB medium containing 50 μg/mL kanamycin and 50 μg/mL thymidine and then induced at 18 °C overnight with 0.1 mM IPTG. After being induced, the cells were harvested by centrifugation. The cell pellet was resuspended in 10 mL of lysis buffer [50 mM NaH_2PO_4, 300 mM NaCl, and 10 mM imidazole (pH 8.0)] and sonicated on ice for 3 min. Centrifugation at 16000 rpm and 4 °C for 30 min yielded a clear lysate, which was incubated with ~2.5 mL of a Ni-NTA slurry at 4 °C for 1 h while being shaken at 200 rpm on a shaker. The lysate/Ni-NTA mixture was loaded into a column, and the flow-through was collected. Following three washes with the buffer described above, the DHFR protein was eluted with elution buffer [50 mM NaH_2PO_4, 300 mM NaCl, and 250 mM imidazole (pH 8.0)]. After dialysis against 25 mM Tris buffer (pH 7.5) with 10% glycerol and 1 mM DTT, the protein solution was concentrated using an Amicon centrifugal filter giving ~20 mg of purified protein.

Steady-State Kinetic Measurement. The overall enzyme turnover rates (k_{cat}) were measured on a Cary 100 BioUV−vis spectrophotometer (Varian Inc.) at 25 °C with a water-jacketed cuvette holder. All reactions were performed in a 1 mL reaction volume in MTEN buffer [50 mM 2-morpholinoethanesulfonic acid, 25 mM tris(hydroxymethyl)aminomethane, 25 mM ethanolamine, and 100 mM NaCl (pH 7.0)] containing 5 mM DTT. The enzyme was preincubated with 100 μM NADPH for 3 min, and then the reaction was initiated via addition of 100 μM dihydrofolate. The decrease in absorbance was monitored at 340 nm ($\Delta\varepsilon_{340}$ = 13.2 mM^{-1} cm^{-1}).

We determined K_M values by having either a substrate or a cofactor at saturation and varying the other over a range of concentrations. The pK_a values were calculated from eqs 1 and 2 (*14*, *15*):

$$k_{obs} = k_{max}/(1 + 10^{pK_a - pH} + 10^{pH - pK_a'} + 10^{pK_a - pK_a'}) \quad (1)$$

$$k_{obs} = k_{max}/(1 + 10^{pK_a - pH}) \quad (2)$$

NADPD Synthesis. For the kinetic isotope effect measurement, [(4′*R*)-^{2}H]NADPH (NADPD) was synthesized by reduction of $NADP^+$ using an $NADP^+$-dependent alcohol dehydrogenase (purchased from Sigma) and 2-propanol-d_8 (purchased from Aldrich) as described in ref *16*.

TMP Inhibition Assay. The measurement of TMP inhibition was performed in the same instrument as described above. A TMP stock solution was dissolved in a 50% DMSO solution and diluted with H_2O. The enzyme was incubated with 100 μM NADPH at varying concentrations of TMP. The reaction was initiated via addition of 10 μM H_2F to the reaction mixture, and the decrease in absorbance due to NADPH consumption was monitored. The IC_{50} was defined as the concentration of the

TMP required to inhibit 50% of the enzyme activity. Determinations of IC_{50} were made by fitting the inhibition data to a single-site sigmoidal model using the nonlinear regression method. The inhibition constants (K_i) were calculated with the equation $K_i = IC_{50}/(1 + [S]/K_M)$ as previously described (*17*).

Stopped-Flow Measurement for Pre-Steady-State Kinetics. All transient or pre-steady-state kinetic data were obtained by using a stopped-flow apparatus (Applied Photophysics Ltd.). Kinetic measurements were taken by exciting enzyme tryptophans at 290 nm, and the resulting fluorescence was monitored using a 320 nm cutoff filter or the FRET resulting from the cofactor fluorescence at 450 nm. The data were analyzed by single-exponential curve fits, giving the observed rate. Ligand dissociation rates were measured by the competition method (*12*). The ligands and traps used in these experiments can be found in Results.

Thermodynamic Dissociation Constants. The equilibrium dissociation constants (K_D) were measured by the quenching of the intrinsic protein fluorescence as a function of ligand concentration using a Flouromax-2 or a Flouromax-4 (Horiba Jobin Yvon) spectrofluorometer. All the titration experiments were conducted in MTEN buffer (pH 7.0) containing 2 mM DTT. spDHFR has three tryptophan residues, which enables the measurement of tryptophan fluorescence at 340 nm from excitation at 290 nm. Enzyme concentrations were typically 25−100 nM. The fluorescence data were corrected for the inner filter effects and fit as described previously (*12*, *18*).

Crystallization and X-ray Data Collection. Robotic screening was done with 500 commercial screen conditions using the Phoenix crystallization robot. Crystals of the Sp9 mutant grew under two conditions: (1) 1 M lithium chloride, 0.1 M sodium citrate (pH 4.0), and 20% PEG6K and (2) 1 M lithium sulfate, 0.1 M Tris (pH 8.5), and 0.01 M nickel chloride. Manual drops set up with the former condition resulted in 90 μm crystals that grew in 4−5 days. The crystals were screened using a home X-ray source consisting of a Micromax 007 X-ray generator and Saturn 944+ CCD detector equipped with Varimax HF optics. The peak harvest time for crystals was 7−10 days. Sucrose saturated in mother liquor was found to be the most suitable cryo-condition giving the best diffraction. X-ray diffraction data to 1.95 Å were collected at the home source. A 145 μm crystal of the wild-type protein grew from 30% PEG MME (polyethylene glycol monomethyl ether) 5000, 0.1 mM MES (pH 6.5), and 0.2 M ammonium sulfate in 4−6 weeks. A 3.3 Å low-resolution X-ray data set was collected with this crystal.

Crystal Structure Solution and Refinement. (*i*) *Sp9 Mutant.* Data collection and processing were conducted using the Rigaku Crystalclear software (CrystalClear: An Integrated Program for the Collection and Processing of Area Detector Data, Rigaku Corp., 1997−2002). The crystallographic parameters are listed in Table 1. Further data processing and molecular replacement calculations were done with Phaser in the CCP4 package (*19*). Sequence alignment of *S. pneumoniae* DHFR (spDHFR) and *Bacillus stearothermophilus* DHFR (PDB entry 1ZDR) (*20*) with 42% sequence identity was the best available molecular replacement model in the Protein Data Bank. Phaser with a 1ZDR monomer and not a dimer provided a solution for both molecules in the *P*21212 space group. The initial molecular replacement phases were improved by using the Phenix package (*21*). Density modification using solvent flattening and NCS averaging options were used. The electron density maps were visualized in Coot (*22*). Simulated annealing refinement using CNS (*23*, *24*) helped in overcoming phase bias. Coot and CNS were iteratively used for model correction and refinement. Model stereochemistry was checked using the Molprobity online server (http://molprobity.biochem.duke.edu/). The final *R*-factors after optimization of weights for refinement in the CNS package are as follows: $R_{cryst} = 0.237$, and $R_{free} = 0.274$. The PDB entry for Sp9 is 3IX9.

Table 1: Crystallographic Parameters

unit cell parameters (Å)	$a = 61.838$, $b = 93.639$, $c = 71.367$
space group	*P*21212
no. of reflections observed	67597
no. of unique reflections	28610
linear merging *R*-factor (%)	10.2
resolution of native data (Å)	1.95
no. of molecules per asymmetric unit	2
final R_{cryst}/R_{free} (%)	23.7/27.4
no. of protein atoms	2764
no. of water molecules	306
ligand molecules	2 methotrexate and 2 NADPH
rmsd for bonds (Å)	0.01
rmsd for angles (deg)	1.52

(*ii*) *Wild Type.* The wild-type protein crystal diffracted to 3.3 Å with cell dimensions of 134.27, 134.27, and 219.88 Å in the hexagonal *P*6/*P*3 family of space groups. There are six to eight monomers in the asymmetric unit, and this high number along with the low resolution of the X-ray data posed difficulty in the molecular replacement structure solution.

RESULTS AND DISCUSSION

Kinetic Characterization of spDHFR. (*i*) *Steady-State Kinetics.* Tables 2 and 3 summarize the kinetic parameters for spDHFR and its mutant Sp9 construct. The k_{cat} of spDHFR at pH 7.0 is 2.5-fold faster than that for *E. coli* DHFR (*12*). The overall turnover rate constant is 31.5 s^{-1} and exhibits a $(k_{cat})^H/(k_{cat})^D$ of 2.4 at pH 7.0 (Table 2A). The kinetic isotope effect (KIE) value of 2.4 in spDHFR suggests that the hydride transfer step is at least partially rate-limiting in the catalytic cycle even at neutral pH. Moreover, in stopped-flow protocols, a pre-steady-state burst of product was not observed for the spDHFR. Its absence is consistent with the hydride transfer step or a preceding step being rate-limiting followed by a subsequent rapid step so that product does not accumulate during the first turnover. On the other hand, the mutant Sp9 enzyme exhibits a KIE value of 1.1 that argues for the rate-limiting step no longer being the chemistry step, even though the latter's nine mutations decrease the catalytic activity of the enzyme by a factor of 8. The presence of a burst with a small amplitude implicates a slower product (H_4F) dissociation step contributing to the overall turnover rate, but further assessment of each individual step in the catalytic cycle was hampered by the weak FRET signal.

The K_M values of NADPH and H_2F for the wild-type spDHFR and the mutant Sp9 were measured (Table 2B). The K_M values for the wild-type spDHFR were at least 1 order of magnitude higher than those for the Sp9 mutant that showed full enzyme activity even at a limiting low concentration of 0.63 μM H_2F, consistent with a much lower K_M value for this substrate. It is not surprising to observe tighter binding of the ligand to the Sp9 mutant because the Sp9 mutant DHFR has Val100 whereas the wild-type spDHFR has Leu at this position. This result is in accord with a previous finding (*10*, *11*) that suggested the steric size of the amino acid side chain at position 100 affected ligand

Table 2: Kinetic Parameters for the *S. pneumoniae* DHFR and the Mutant Sp9 at pH 7.0 in MTEN Buffer

(A)

enzyme	k_{cat} (s^{-1})	$k_{\text{cat(NH)}}/k_{\text{cat(ND)}}$	$K_{\text{d(NADPH)}}$ (μM)
S. pneumoniae	31.5 ± 2.5	2.4 ± 0.03	0.21 ± 0.013
Sp9	3.8 ± 0.93	1.1 ± 0.05	0.16 ± 0.058
E. coli (wild-type)	12.0[a]	1.0[a]	0.33[a]

(B)

enzyme	$K_{\text{M(NADPH)}}$ (μM)	$K_{\text{M(H}_2\text{F)}}$ (μM)	k_{cat} (s^{-1})	$k_{\text{cat}}/K_{\text{M(NADPH)}}$ ($\mu M^{-1}\ s^{-1}$)	$k_{\text{cat}}/K_{\text{M(H}_2\text{F)}}$ ($\mu M^{-1}\ s^{-1}$)
S. pneumoniae	15.7 ± 4.6	4.4 ± 0.95	31.5 ± 2.5	2.0	7.2
Sp9	0.75 ± 0.3	< 0.63	3.8 ± 0.9	5.0	> 6.0
E. coli	4.8[a]	0.7[a]	12.0[a]	2.5	17.1

[a] Taken from ref *12*.

Table 3: Enzyme Inhibition Data for Trimethoprim against the *S. pneumoniae* and Sp9 Mutant DHFR

enzyme	K_i (nM)	IC_{50} (nM)
S. pneumoniae	147 ± 49	480
Sp9	3.9 ± 0.5	130

binding and its substitution may confer drug resistance on the enzyme. In the case of the Sp9 mutant, substitution with Val accommodates improved binding by the substrate and cofactor, reflecting less steric clash between the substrate and position 100. Note that the specificity constants (k_{cat}/K_M) of the Sp9 mutant enzyme are comparable to those of the wild type since the decreased catalytic activity of the Sp9 mutant enzyme is offset by the increased binding affinity for the ligands.

The K_i values for trimethoprim were determined as shown in Table 3. Changes in the catalytic efficiency caused by TMP binding were examined by incubating the enzymes with varied concentrations of TMP. Sp9 containing Val100 has a K_i value of 3.9 nM, whereas wild-type spDHFR with Leu100 has a value of 147 nM. The tighter binding of TMP to the Sp9 mutant DHFR than to wild-type spDHFR presumably arises from an increased level of accommodation of the drug because of the Val100 substitution, so that Sp9 is trimethoprim sensitive.

(*ii*) *NADPH Binding to spDHFR*. Fluorescence spectroscopy was employed to probe the binding of ligands to spDHFR and the Sp9 mutant. Titration of those proteins with NADPH resulted in a quenching of their intrinsic emission and provided the thermodynamic dissociation constants summarized in Table 2A. NADPH binds more tightly (ca. 2-fold) to spDHFR than *E. coli* DHFR. The Sp9 DHFR mutant retained this tight binding with NADPH, which strongly suggests that those nine mutations did not significantly perturb the enzyme structure.

The NADPH dissociation constant based on the relaxation method to measure the on and off rates was 1.5 μM (Table 4), while the value from the equilibrium titration method was 0.21 μM. It is not uncommon to observe a difference between the two methods; the same is true for the *E. coli* enzyme, albeit to a lesser extent. The DHFR enzyme is known to have multiple conformations (*25*) in the absence of NADPH, with the ligand binding to a preferred conformation. In the case of the *E. coli* DHFR, the apoenzyme exists in two conformational states (E_w and E_t) with an affinity difference for NADPH of >100-fold. The isomerization process from inactive conformer (E_w) to the active conformer (E_t) was found to occur with a half-life of 71 s, while the conversion of E_w NADPH to E_t NADPH occurs with a half-life of 30 s (*26*). At equilibrium in the presence of NADPH, the enzyme conformations with tighter binding to NADPH will be predominant. Consequently, transient kinetic measurements with spDHFR listed in Table 4 may include the rates of isomerization between conformers in addition to ligand binding and dissociation, leading to a disparity between the methods. Kinetic traces for NADPH binding fit to a single exponential and were not improved by a double-exponential curve fit. One of the stopped-flow traces is presented in Figure 2A. Presumably, the data shown here were not resolved to a double exponential within the observed time scale.

Quenching of the intrinsic fluorescence with H_2F binding in equilibrium did not produce data that can be fitted to a binding curve. The fluorescence signal was decreased upon addition of H_2F, but the data were difficult to fit, which appeared to be related to slow conformational fluctuations upon binding.

(*iii*) *Transient-State Kinetics*. Since dissociation of tetrahydrofolate (H_4F) is the rate-limiting step in the wild-type *E. coli* DHFR reaction pathway (*12*), the dissociation of ligands from various complexes was assessed for spDHFR by a competition method (Table 5). The enzyme−ligand complex is mixed with a large excess of a second ligand (e.g., methotrexate, NADPH, or $NADP^+$). These two species of ligands compete for a common binding site so that under these conditions the dissociation rate of the bound ligand is equal to the observed rate (*12*).

Scheme 1 depicts the kinetic scheme for spDHFR compared to *E. coli* DHFR incorporating the data presented above. In spDHFR, the dissociation of H_4F from either $E{\cdot}H_4F{\cdot}N^+$ or $E{\cdot}H_4F$ is much slower than k_{cat}. Moreover, the rate of dissociation of $NADP^+$ from the $E{\cdot}H_4F{\cdot}N^+$ ternary complex, which is on the pathway to form $E{\cdot}H_4F{\cdot}NH$, is much faster ($> 250\ s^{-1}$) than that of dissociation of H_4F from the same ternary complex ($5.7\ s^{-1}$). This restricts the reaction pathway to the same inner loop of the reaction scheme as observed for *E. coli* DHFR. The rate of dissociation of H_4F from the $E{\cdot}H_4F{\cdot}NH$ ternary complex (FRET) could not be determined by the competition method due to the weaker signal of the ternary complex and suspected high off rates.

Since the rates for the chemistry step ($E{\cdot}NH{\cdot}H_2F \rightarrow E{\cdot}N^+{\cdot}H_4F$) and product dissociation step from the $E{\cdot}H_4F{\cdot}NH$ ternary complex could not be determined accurately, they were simulated by Dynafit (*27*) within the constraints imposed by

Table 4: Kinetic Constants for Binding of NADPH to *S. pneuminiae* DHFR in MTEN Buffer at 25 °C (relaxation method)

	$k_{on(NADPH)}$ (μM^{-1} s^{-1})	$k_{off(NADPH)}$ (s^{-1})	k_{off}/k_{on} (μM)
S. pneumoniae	11.9 ± 1.4	18.0 ± 3.2	1.5
E. coli DHFR	20.0[a]	3.5[a]	0.18[a]

[a] Taken from ref *12*.

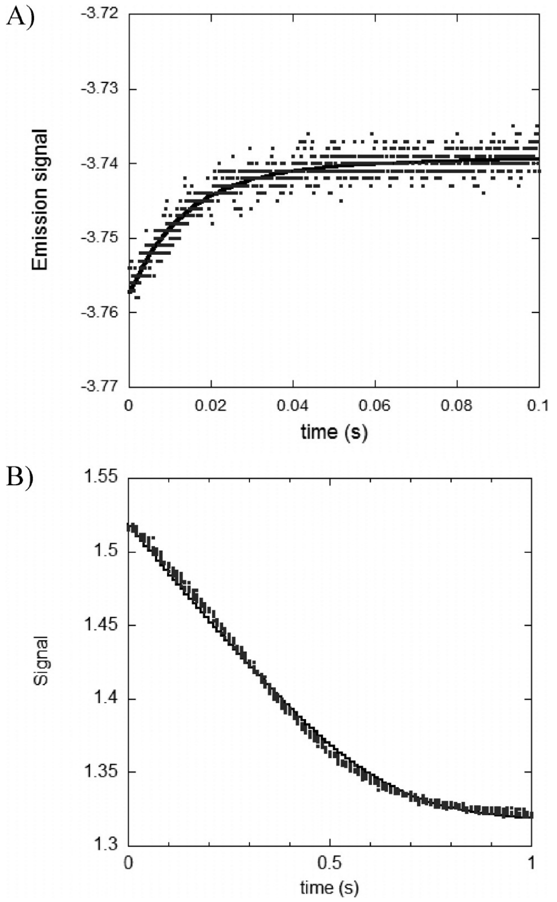

FIGURE 2: (A) Stopped-flow time course for the binding of 0.5 μM spDHFR with 5 μM NADPH at pH 7.0. The solid line represents the fit of the data to a single-exponential function. (B) Measurement of the time course for the hydride transfer rate catalyzed by spDHFR as monitored by stopped-flow absorbance. spDHFR was preincubated with NADPH, and the reaction was initiated by mixing with H_2F. The final concentrations were 5, 100, and 100 μM for the enzyme, NADPH, and H_2F, respectively, at pH 7.0. The solid line represents the fit of the absorbance data by using Dynafit under the given experimental condition, and kinetic parameters derived from this simulation are summarized in Table 6.

k_{cat} and the other dissociation constants (Table 6). Refer to Scheme 2 for the definitions of the rate constants. All the initial values for each of the rate constants were designated as adjustable fitting parameters except for k_0 and k_{01} that were obtained from binding experiments. We started with initial values based on those of the *E. coli* DHFR, but no good fit was obtained. We then varied each rate constant one at a time through a wide range of initial values. The ranges of initial values as adjustable parameters that generated good curve fits are as follows: k_1 = 40 μM^{-1} s^{-1}, k_{11} = 40 s^{-1}, k_2 = 32 s^{-1}, k_{21} = 0.1 s^{-1}, k_3 = 200−500 s^{-1}, k_4 = 8−10 μM^{-1} s^{-1}, k_{41} = 100−200 s^{-1}, k_5 = 150−1000 s^{-1}, and k_{51} = 10−40 μM^{-1} s^{-1}.

The simulation result was consistent with our experimental data, showing that the hydride transfer step or a preceding step presumably involving a conformational change is participating as a rate-limiting step in spDHFR. Since no pre-steady-state burst was observed under multiple-turnover conditions by a stopped-flow measurement (Figure 2B), the rate of dissociation of H_4F from the E·H_4F·NH complex was estimated to be greater than 1600 s^{-1}. The measured rate of dissociation of $NADP^+$ from the E·N^+·H_4F ternary complex by the stopped-flow measurement was close to the experimental detection limit (> 250 s^{-1}). The value estimated from Dynafit simulation was 400 ± 79 s^{-1}, which is reasonable since it is difficult to obtain an accurate rate constant around the experimental limit. The binding constants for the E·H_4F·NH complex formed from binary complexes (from either E·H_4F or E·NH) were suggested to range from 70 to 100 μM based on the k_{off} and k_{on} ratio. The calculated specificity constant [$k_{cat}/K_{M(H_2F)}$] obtained by using the following equation was ~4 μM^{-1} s^{-1}, which is comparable to the value of 7.2 μM^{-1} s^{-1} from the experiment, where K_M = $(k_{11}k_3)/(k_1k_2)$.

Our simulation data with the simplified model shown in Scheme 2 produced larger error ranges for the fit along with a certain residual pattern. It is not unusual to see this uncertainty with nine variable parameters, which results from a lack of experimental constraints due to the weaker fluorescence signal that had impeded further investigation for individual steps. Nonetheless, we have demonstrated that all of the independent fits with varied initial guesses converged to a certain range of rate constants listed in Table 6. We are aware that this postulated fitting model may have limitations (including significant error ranges for the fit along with a certain residual pattern), but we intended to demonstrate that the resultant model is consistent with our experimental data supporting the absence of a pre-steady-state burst and that the hydride transfer or a preceding step limits the overall turnover rate. We can exclude the pathway in which product dissociation is a rate-limiting step as observed in *E. coli* DHFR. Taken together, the experimental and simulation

Table 5: Dissociation Rate Constants for Ligands from Wild-Type *S. pneumoniae* DHFR and the Sp9 Mutant at 25 °C in MTEN Buffer at pH 7.0

enzyme	ligand	enzyme species	trapping ligand	k_{off} (s^{-1}) at pH 7.0
S. pneumoniae (wild type)	H_4F	E·H_4F·NH	MTX	ND[a]
		E·H_4F·N^+	MTX	5.7 ± 0.4
		E·H_4F	MTX	3.8 ± 0.1
	$NADP^+$	E·H_4F·N^+	NADPH	> 250[b]
	NADPH	E·H_4F·NH	$NADP^+$	ND[a]
Sp9	H_4F	E·H_4F·NH	MTX	ND[a]
		E·H_4F·N^+	MTX	12.0 ± 1.6
		E·H_4F	MTX	6.7 ± 0.2

[a] Not determined due to the weaker signal. [b] The value is close to the experimental detection limit and estimated to be 400 s^{-1} from the simulation.

Scheme 1: Representation of the *E. coli* DHFR Reaction (*12*) and *S. pneumoniae* DHFR at pH 7.0[a]

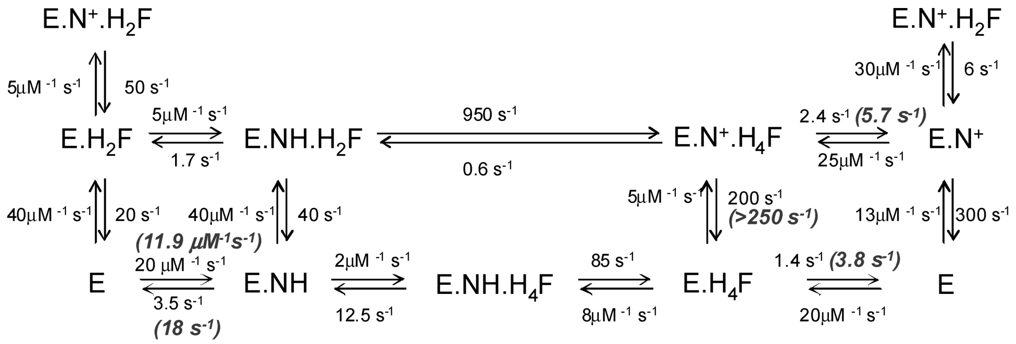

[a] Highlighted with bold italic are the rate constants measured from experiments for *S. pneumoniae* DHFR. Abbreviations: E, DHFR; NH, NADPH; H_2F, 7,8-dihydrofolate; H_4F, tetrahydrofolate; N^+, $NADP^+$.

Scheme 2: Representation of the spDHFR Reaction[a]

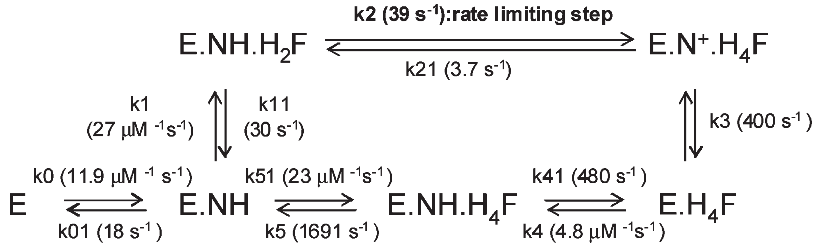

[a] The data were obtained from simulated fits as described in Table 6.

Table 6: Statistics of the Simulated Fits for the spDHFR Reaction Pathway by Dynafit (*27*)

	k_1 (μM^{-1} s^{-1})	k_{11} (s^{-1})	k_2 (s^{-1})	k_{21} (s^{-1})	k_3 (s^{-1})	k_4 (μM^{-1} s^{-1})	k_{41} (s^{-1})	k_5 (s^{-1})	k_{51} (μM^{-1} s^{-1})
fit 1	26.2	34.0	38.5	0.0	299.4	5.6	649.6	2022.0	22.1
fit 2	25.9	27.3	40.0	14.4	447.3	4.7	477.6	1680.0	16.4
fit 3	25.6	28.9	38.1	0.0	447.8	4.7	445.5	1885.0	14.5
fit 4	19.5	48.3	38.8	0.0	461.9	4.5	411.2	839.6	22.3
fit 5	37.1	12.5	40.0	8.0	446.1	4.7	402.4	1540.0	43.7
fit 6	29.0	33.0	39.6	0.0	298.9	4.9	493.4	2180.0	19.8
mean	27.2	30.6	39.2	3.7	400.2	4.8	480.0	1691.1	23.1
standard deviation	5.8	11.6	0.8	6.1	78.5	0.4	90.4	476.3	10.5

results suggest that the $E\cdot H_4F\cdot NH$ ternary complex of spDHFR is less stable than in *E. coli* DHFR.

(*iv*) *pH Dependence of Activity*. The pH dependencies of wild-type spDHFR and the Sp9 mutant activity were investigated (Figure 3). The k_{cat} values of these two enzymes over the broad pH range showed a pH dependence of enzyme activity. A single maximum is observed at pH ~7.0 for both enzymes. Bacterial DHFRs generally exhibit an optimum activity in the pH range of 6.0−6.5, while the enzymes from mammalian sources show optimum activity at pH 4.5−5.5 (*28*). In the case of the *E. coli* DHFR, the k_{cat} was pH-independent below pH 7.0 which was rationalized by the need for protonation of Asp27 in the active site (*29*). In contrast to *E. coli* DHFR, the maximum activity of the *S. pneumoniae* enzymes at pH 7.0 implies that there might be an ionizable residue participating in the enzyme turnover. Two pK_a values of 6.2 and 7.9 were obtained by fitting the pH profile curve to eq 1 as described in Materials and Methods (Figure 3A) (*14*). We surmised that the pK_a of 6.2 may be attributed to the ionization of His33 placed at the active site of DHFR by our structural analysis. A mutant enzyme of spDHFR that has Phe at position 33 (H33F) exhibits a pH dependence profile similar to that of *E. coli* DHFR (Figure 3B); the k_{cat} values from pH 6.0 to 7.5 are pH-independent with a k_{cat} value of 22.8 ± 2.2 s^{-1} and decrease in basic pH regions with a pK_a of 8.2. This result suggests that His33 is participating in the active site as another ionizable group in spDHFR.

Analysis of the observed pK_a of 7.9 draws on similar observations for other DHFR species. First, the chemistry steps in *E. coli*, *Lactobacillus casei*, and human DHFR have values of 950, 430, and 1360 s^{-1}, respectively (*12*, *30*, *31*). The k_{cat} values in Figure 3 are 31.5 and 22.8 s^{-1} for the wild type and the His33Phe mutant DHFR and are far slower than the usual value for the chemistry step. Second, the pK_a value observed in plots of the actual chemical step ($k_{hydride}$) for the *E. coli* DHFR is 6.5, shifted down by 1.9 units from the value of 8.4 in a plot of k_{cat} versus pH for the *E. coli* enzyme. This shift results from a change in the rate-limiting step from the chemical step at high pH (> 8.4) to dissociation of H_4F from the $E\cdot NH\cdot H_4F$ complex at low pH (< 8.4).

For spDHFR, the rate of the chemical step could not be measured by the pre-steady-state kinetic method because of the

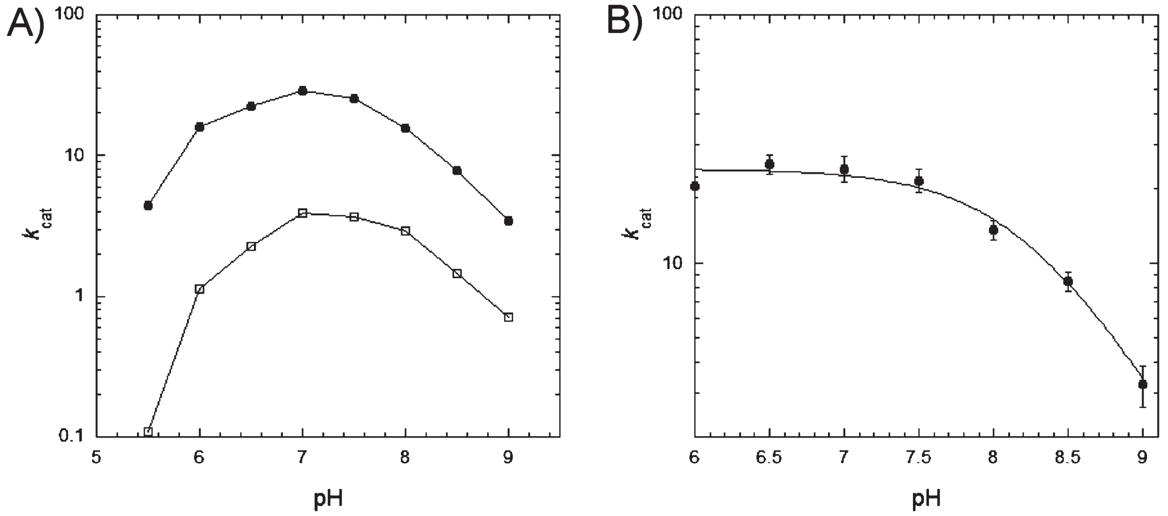

FIGURE 3: pH−rate profiles at 25 °C in MTEN buffer. (A) Both *S. pneumoniae* DHFRs [wild type (●) and Sp9 DHFR (□)] exhibited maximum activities at pH 7.0. The two pK_a values of *S. pneumoniae* DHFR were calculated to be 6.2 and 7.9 from the curve fit eq 1 (*14*). (B) The His33Phe mutant DHFR exhibited a pH profile similar to that of *E. coli* DHFR from ref *12* with a pK_a of 8.2 when fitted to eq 2 (*15*).

absence of biphasic kinetics. However, measurements of the isotope effect k_H/k_D (NADPH vs NADPD) for the spDHFR enzyme varied in the following order: 1.0 (pH 6.0), 2.4 (pH 7.0), 3.8 (pH 9.0). These results support the fact that the k_{cat} for spDHFR at pH 7 incorporates the combination of a slow conformational change ($E\cdot NH\cdot H_2F \rightarrow E'\cdot NH\cdot H_2F$) prior to the chemistry step and the actual hydride transfer step. At lower pH, the intrinsic hydride transfer rate should be much higher than that of k_{cat}, so that a conformational change step limits the overall catalytic turnover as shown with a KIE value of 1.0. At higher pH, the chemical step limits the overall catalytic turnover with a KIE value of 3.8. Consequently, the pK_a shift observed in spDHFR is derived from a change in the rate-limiting step from one of conformational change prior to the chemistry step to one involving chemistry.

The kinetic studies described above revealed that the kinetic behavior of spDHFR is significantly different from that of *E. coli* DHFR; the H_4F dissociation step which was the rate-limiting step in the *E. coli* DHFR was accelerated by at least 100-fold in the spDHFR. The pH dependence of the catalytic efficiency of spDHFR implicates different catalytic residue(s) in the binding site. The influence of the histidine appears at lower pH (pK_a = 6.2), and its absence does not affect the rate observed for the wild type and His33Phe mutants at the maxima in k_{cat} (Figure 3B). Consequently, it does not appear to facilitate the rate of the conformational step ($E\cdot NH\cdot H_2F \rightarrow E'\cdot NH\cdot H_2F$). The most likely role of the histidine is revealed by the X-ray structure discussed below.

Description of the Sp9 DHFR Structure. (*i*) *Overall Fold and Mobility*. We discuss now the details of the crystal structure of the Sp9 DHFR mutant complexed with methotrexate and NADPH. The 1.95 Å structure of Sp9 has good geometry and a final *R*-factor and an R_{free} of 23.7 and 27.4%, respectively. The stereochemical quality of the protein structure was evaluated by the Molprobity server. The average *B*-factors are 29 Å^2 for the main chain and 33 Å^2 for the side chain and water molecules. The crystallographic parameters are listed in Table 1 in Materials and Methods. The σ value for the electron density is 1.5.

DHFRs from different species are known to have an overall low level of sequence identity of almost 20% but share the same general fold, a central β-sheet with four surrounding α-helices. The overall fold of the Sp9 mutant is similar to the fold of *E. coli* DHFR (*32*) as seen from an overlay diagram of the two monomers (Figure 4A). The two structures superimpose well with an rmsd of 1.02 Å for 148 backbone C-α atoms. The central β-sheet of Sp9 DHFR consists of eight parallel and two antiparallel strands. While the *E. coli* protein is a monomer, the Sp9 mutant is a tight dimer (Figure 4B) with a buried surface area of 708 Å^2 [calculated with Areamol, part of the CCP4 package (*19*)]. Molecular replacement with the dimer search model of *B. stearothermophilus* DHFR [PDB entry 1ZDR (*20*)], with which the spDHFR sequence shares the most homology (42% identical, 61% positives, and 2% gaps), failed to determine the structure of the Sp9 as the molecules dimerize in different orientations. Molecular replacement with a monomer of 1ZDR worked in the determination of the structure. Blast searches of spDHFR against DHFRs whose structures are known show the least homology with human DHFR (PDB entry 1U71) (*33*) (26% identical, 44% positives, and 12% gaps) yet good structural overlap.

The loops (Met20 loop, residues 9−24; βF−βG loop, residues 117−131; βG−βH loop, residues 146−148) crucial in catalysis and substrate binding exhibit higher mobility in the *E. coli* DHFR than in the Sp9 DHFR as seen from a comparison of their relative crystallographic temperature factors (Figure 4A). Of the three loops, the Met20 loop and the βG−βH loop reside on the dimer interface, accounting for their reduced mobility. The spDHFR Met20 loop is in the closed conformation. The two monomers of the dimer superimpose on each other well with an rmsd of 0.62 Å. Surface residues 69−76 and 132−139 show the most variability in its conformation. These regions are, however, not in the vicinity of the active site.

(*ii*) *Wild-Type DHFR Model*. The wild-type protein crystal diffracted to 3.3 Å and has six to eight monomers in the asymmetric unit. This high number along with the low resolution of the X-ray data posed difficulty in determining the structure through the molecular replacement method. Through molecular modeling, we have introduced the wild-type amino acids at the nine mutated positions of the Sp9 structure (Figure 1C). The residues were relaxed into their minimum-energy conformers using Coot and remained close to the orientations of the corresponding Sp9 DHFR residues. The overall model was

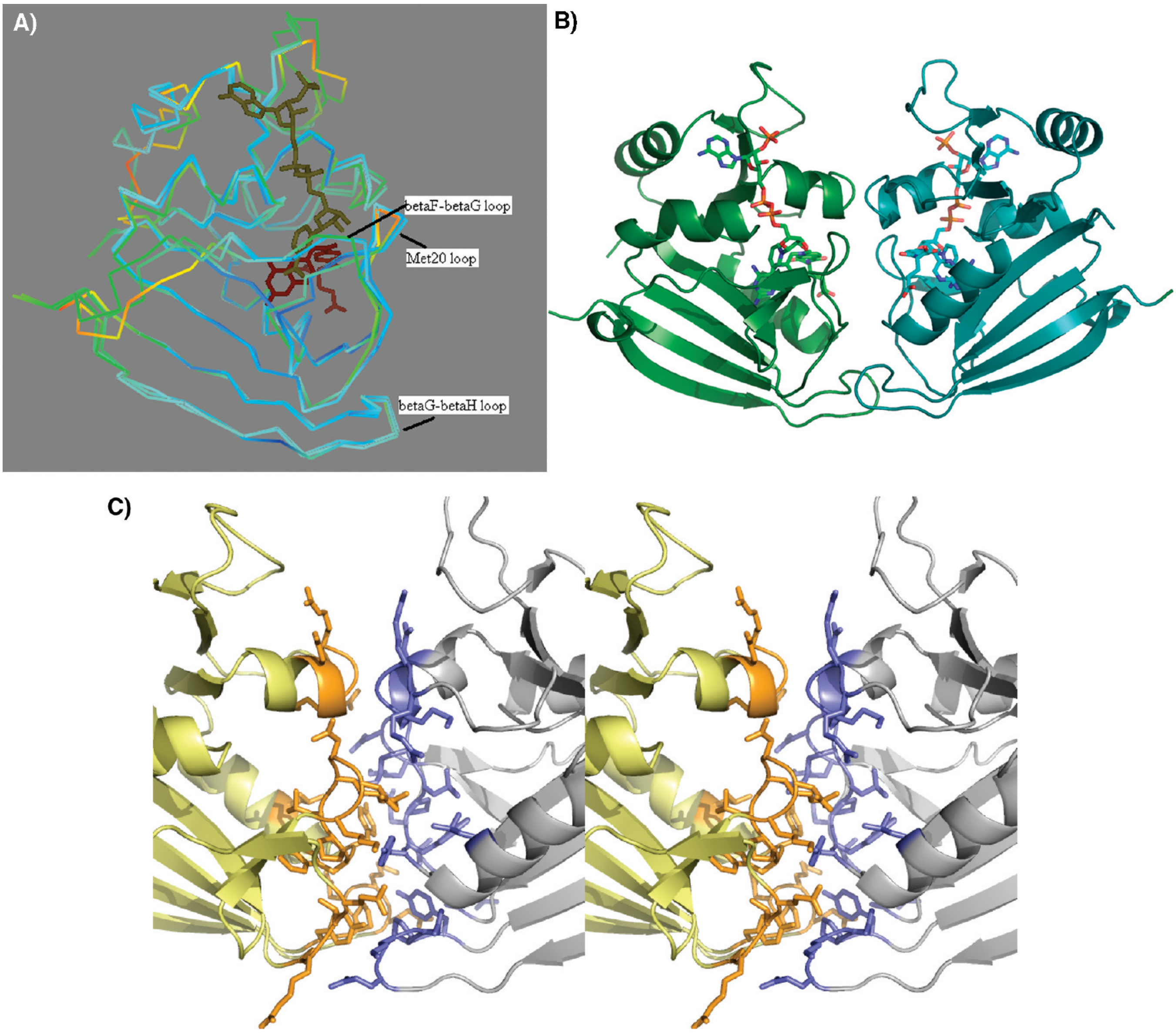

FIGURE 4: (a) Superposition of the *E. coli* and Sp9 DHFR monomers colored according to their temperature factors, with red representing mobile regions and blue the rigid regions. The substrate binding loops and helix in the *E. coli* structure seem to be more flexible compared to the Sp9 mutant. (b) Cartoon representation of the Sp9 DHFR dimer. (c) Stereoview of the dimer interface. Residues are shown in stick representation.

energy minimized using the GROMOS 43B1 force field in Swiss-pdbviewer. Eight of the nine mutations are on the surface of the protein, with one mutation (Val100 to Leu) in the active site. The locations of the nine mutations are presented in Figure 1C. While the role of the V100L mutation in the active site associated with ligand binding is evident from the X-ray structure, the role of the eight other mutations located on the surface is not clear. The surface mutations may be responsible for the difference between the crystallization properties of the two crystal forms and their X-ray diffraction. We surmise that altered charge distribution on the surface of the protein may contribute to better crystal packing in Sp9.

(*iii*) *Active Site Residues*. We have compared the structures of the Sp9 mutant (ternary complex with methotrexate and NADPH) and the published *E. coli* DHFR structure [PDB entry 1RH3 (*32*), also a ternary complex with methotrexate and NADPH]. Between the published *E. coli* and the Sp9 active site structures, the change of His33 for Trp is the most noteworthy. This is consistent with our kinetic observations of a pH dependence in k_{cat} for the wild-type spDHFR. An inspection of the active site shows that His33 interacts with active site residues and the pteridine ring of the methotrexate through a hydrogen-bonded network involving a water molecule [water 22 (Figure 5A)]. A superposition diagram of the active sites of the *E. coli* (PDB entry 1RH3) (*32*) and *S. pneumoniae* Sp9 structures is shown in Figure 5B.

Eight of the residues in the active site are different from those of *E. coli* DHFR. A listing of the active site residues with the spDHFR residue first and the *E. coli* next follows: Trp9/Ala6, Leu23/Met20, Glu30/Asp27, His33/Trp30, Phe34/Phe31, Val100/Ile94, Phe106/Tyr100, and Ile160/Phe153. Most residues have similar physical and chemical properties, but there is a dramatic difference between His33 and Trp30. His33 appears to stabilize the hydrogen bonding network to the carboxylate ion of Glu30 (Asp27 in *E. coli* DHFR) through water molecule 22 as well as the hydroxyl group of Thr119. In the case of *E. coli* DHFR, the replacement of His33 with Trp30 explains the pH independence below pH 7 for *E. coli* DHFR. Although the geometric configurations of the imidazole group of His33 and

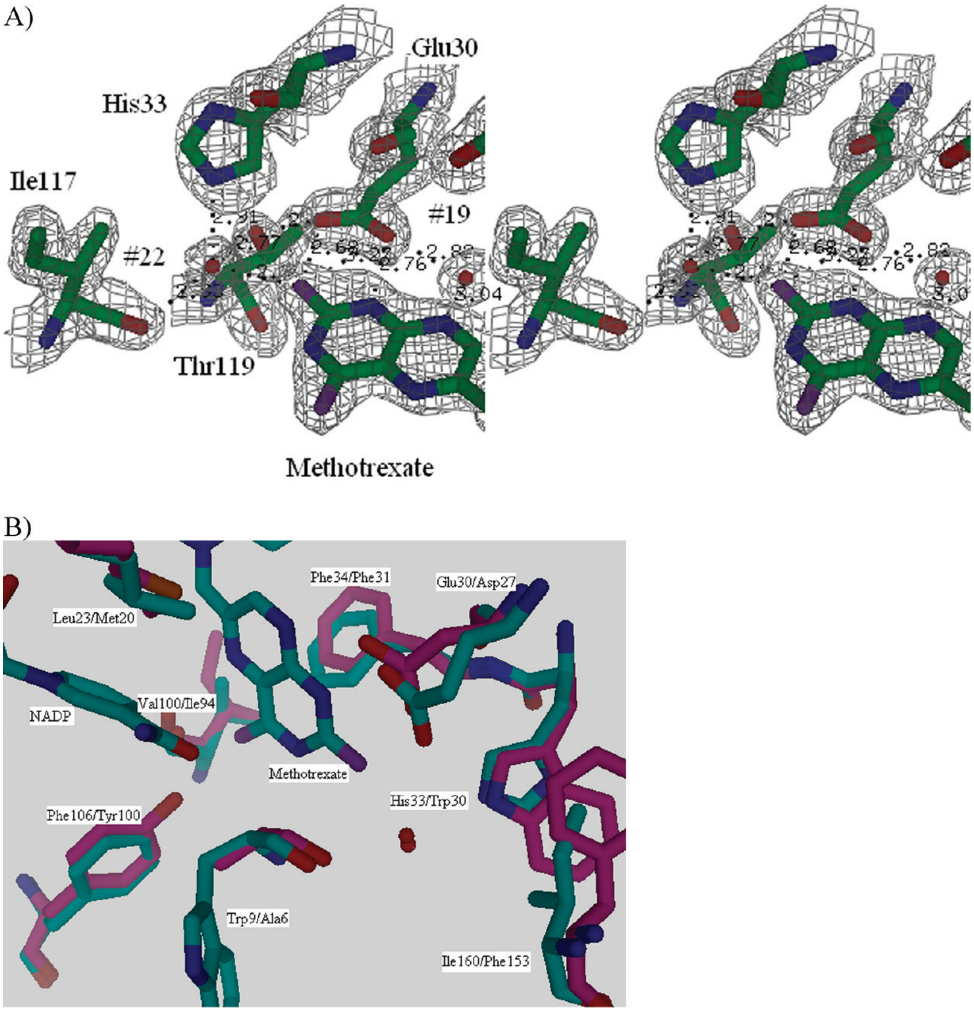

FIGURE 5: (A) Electron density shown as a stereoview for the active site region of the Sp9 DHFR mutant, including His33 and Glu30 residues (σ value of 1.5) and (b) superposition of *E. coli* (pink) and spDHFR (cyan), where eight of the active site residues differ. The labeled amino acids are in the order *S. pneumoniae* DHFR Sp9 followed by the *E. coli* DHFR residue. Note that spDHFR has 168 amino acids while ecDHFR has 159. This causes different numbering when comparing the two sequences.

indole ring of Trp30 are similar, the nonionizable N5 atom from the indole group of Trp30 retains its hydrogen bonding network in the acidic pH region whereas the hydrogen bonding network is altered by protonation of His33 in spDHFR. Guided by this X-ray result, we generated a mutant enzyme of spDHFR that has Phe at position 33 (His33Phe). As expected, this enzyme exhibited no pH dependence in the acidic pH range like *E. coli* DHFR (Figure 3B), confirming the participation of His33 in the hydrogen bonding network.

The role of His33 is equivocal. The imidazole ring of His33 is braced with two hydrogen bonds associated with two water molecules (HOH#22 and HOH#93). At low pH, protonation of His33 might disrupt these hydrogen bonds, affecting the transfer of a proton to the N5 position of H_2F from Glu30 or the equilibrium protonation stage of the $E\cdot NH\cdot H_2F$ complex thus slowing k_{cat}. The KIE measurement supported at low pH a conformational change step for the conversion of $E\cdot NH\cdot H_2F$ to $E'\cdot NH\cdot H_2F$ that alternatively might be inhibited by a protonated histidine. This conformational step likewise may facilitate the proton transfer step as well as the final proton equilibrium to the N5 position within the $E\cdot NH\cdot H_2F$ complex. Since the His33Phe mutant retains k_{cat}, one minimally can conclude that the imidazole does not participate in the N5−glutamate proton transfer process or equilibrium.

Conservation of His33 in the DHFR Superfamily. Composition analysis of the multiple-sequence alignment of 125 DHFR superfamilies (cd00209) was conducted to determine the evolutionary constraints on the active sites of DHFRs. The analysis revealed that the His residue is the most predominant residue in position 33 in the active site (Figure 6). *E. coli* DHFR has Trp, while humans and some organisms (e.g., yeast, fungi, and protozoa) have a Tyr residue in that position. Further analysis of the sequences with His revealed it occurs mostly in bacterial DHFRs; 35 bacterial DHFRs along with one zebrafish and one virus sequence contain His at position 33, so that ∼94% of the sequences with histidine are found in bacteria. In addition, ∼30 of these 35 DHFRs are pathogenic bacteria (∼86%). Consequently, these bacteria have optimized their DHFRs to function at a physiological pH of 7.2−7.4.

Ternary Complex of Wild-Type spDHFR. To rationalize differences in the magnitude of the kinetic steps in the turnover cycle between the *S. penumoniae* and *E. coli* DHFRs, a comparison of the ternary complexes was undertaken. A structure of a complex of *E. coli* DHFR with 5,10-dideazatetrahydrofolate (DDF) and nicotinamide adenine dinucleotide phosphate ($NADP^+$) (PDB entry 1RX6) (*32*) was used as the starting model. The DDF molecule was modeled into the active site of

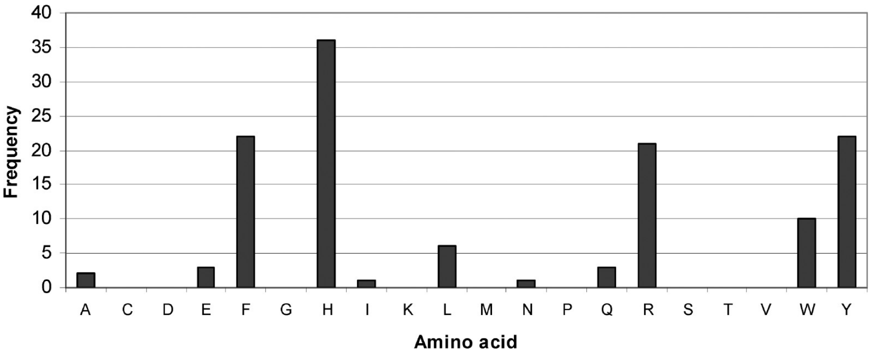

FIGURE 6: Amino acid distribution in the His33 position among members of the DHFR superfamily (cd00209). Further sequence analysis of this DHFR family revealed that the histidine residue is the major occupant of this position (see the text).

A) E. coli

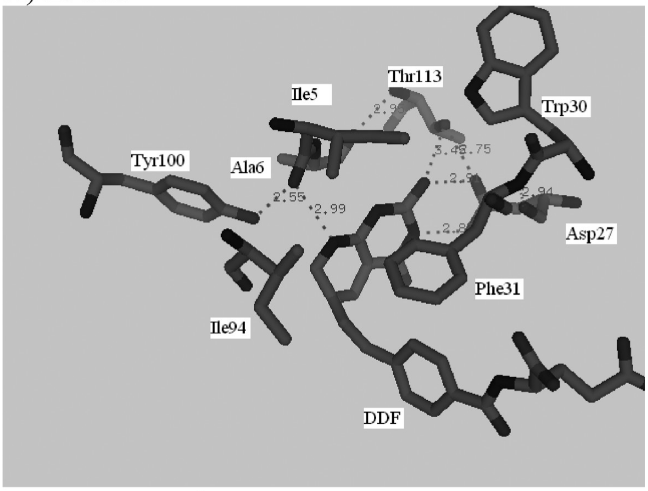

B) S. pneumoniae

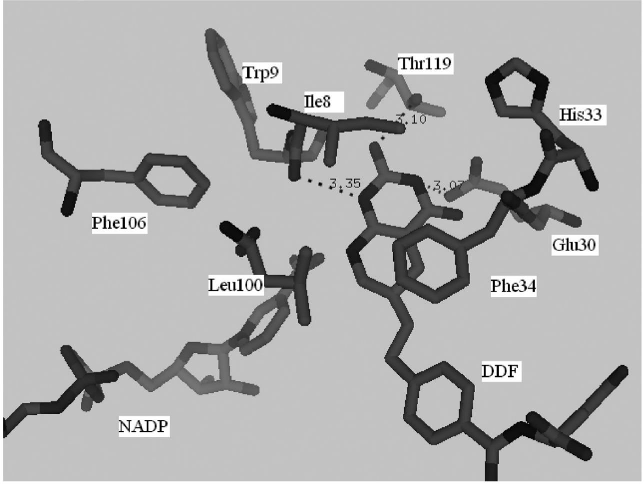

FIGURE 7: Ternary complex as seen in the *E. coli* crystal structure with dideazatetrahydrofolate (DDF) (A) and an energy-minimized model of *S. pneumoniae* with DDF and NADPH (B).

wild-type spDHFR on the basis of a superposition of the two structures using Swiss-pdbviewer. The initial complex was energy minimized using CNS. A comparison of the *E. coli* (Figure 7A) and spDHFR (Figure 7B) ternary complexes showed that the substrate analogue in the *E. coli* active site was more tightly bound than in the *S. pneumoniae* active site. The folate ring and the residues at the active site in the immediate vicinity were stabilized by seven hydrogen bond interactions in the *E. coli* structure versus three hydrogen bonds in the spDHFR (marked as dashes in Figure 7). The two share an equal number of van der Waals contacts. This provides a plausible structural explanation for the weaker binding of H_2F (in terms of K_M = 4.4 vs K_M = 0.7 μM) and the more rapid dissociation of H_4F (>1600 s^{-1} vs 12 s^{-1}). The weaker binding of ligands implicated in this model, however, does not appear to have an impact on the hydride transfer rate that we estimate by extrapolation of k_{cat} in Figure 3B (the decreasing pH limb) to a pK_a of < 7 is >1000 s^{-1}.

Val/Ile100 → Leu Mutation and Trimethoprim Resistance. Earlier studies of trimethoprim resistance in DHFRs have indicated that position 100 is crucial (*10*, *11*) as seen from the structure of *Mycobacterium tuberculosis* DHFR complexed with NADPH and trimethoprim [PDB entry 1DG5 (*34*)]. The trimethoprim molecule is tightly bound in the active site by a stacking interaction with the Phe31 ring and four hydrogen bonds (black dashes in Figure 8) involving residues Ile94, Ile5, and Asp27. The side chains of Ile94 and Phe31 are in van der Waals contact. A superposition of the spDHFR Sp9 mutant onto the active site of *M. tuberculosis* DHFR showed that Val100, Ile8, Phe34, and Glu30 are in superimposable positions. A simple mutation of Val100 to Leu shows that the leucine side chain sterically clashes with the side chains of Ile8 and Phe34 (red dashes in Figure 8) and shifts their positions, thus destabilizing hydrogen bonding and stacking interactions with the trimethoprim molecule. Weaker binding of trimethoprim to Leu100 of DHFR would lead to trimethoprim resistance. The study of inhibition of spDHFRs by TMP (Table 3 and Figure 9) is consistent with the effect of the Leu100 residue in wild-type spDHFR on TMP binding (K_i values of 147 and 3.9 nM for the wild type and Sp9, respectively). The TMP sensitivity of Sp9 appears to be analogous to those of TMP sensitive bacterial DHFRs, suggesting the retention of the hydrogen bonding and stacking interactions with the 2,4-aminopyridine ring of TMP illustrated in Figure 8.

Collectively, the data presented herein have deepened our understanding of the relationship between structure and enzyme catalysis. The kinetic properties of the drug-resistant *S. pneumoniae* DHFRs and the mutant DHFR (Sp9) have been characterized in detail in conjunction with structural analysis from X-ray crystallography. The enzymes exhibit unique kinetic properties that are significantly different from those of *E. coli* DHFR: the rate-limiting step is the hydride transfer step and/or preceding step and not dissociation of H_4F; the pH-dependent kinetics can be assigned to participation of an active site His residue; substitution at the Leu100 position significantly influenced the ligand binding off rate and correlated with trimethoprim

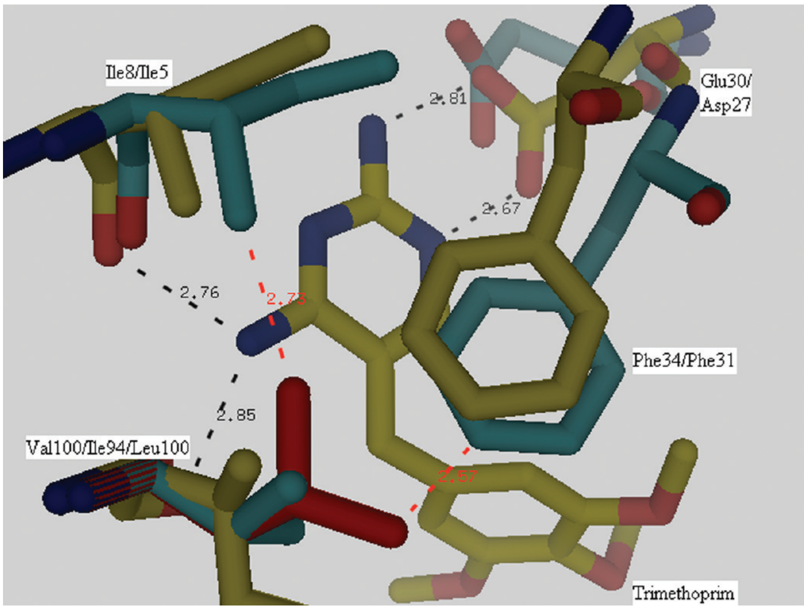

FIGURE 8: Superposition of the *S. pneumoniae* DHFR Sp9 structure and a complex of *M. tuberculosis* DHFR with trimethoprim (PDB entry 1DG5). Val100 in *S. pneumoniae* Sp9 DHFR and Ile94 in *M. tuberculosis* DHFR showed stacking (Phe with the pyrimidine ring of trimethoprim) and hydrogen bond interactions (black dashes). No steric clashes occur. Mutation of Val100 to Leu as seen in the wild-type protein results in a steric clash of the side chains (red dashes). The first numbered label in the figure is the *S. pneumoniae* DHFR Sp9 mutant residue, and the second is 1DG5.

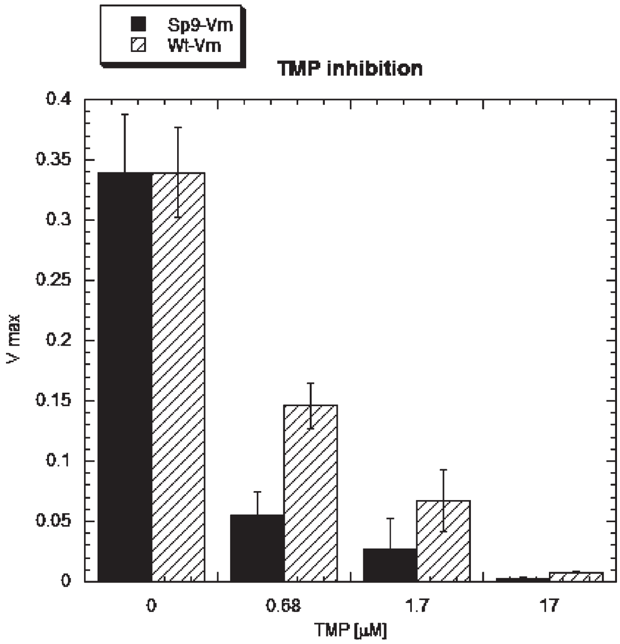

FIGURE 9: *S. pneumoniae* DHFR activity decreased by TMP binding at pH 7.0 in MTEN buffer.

resistance. The insight gained from this work will help in the design of new inhibitors targeting drug-resistant pathogenic bacterial DHFRs.

REFERENCES

1. Hawser, S., Lociuro, S., and Islam, K. (2006) Dihydrofolate reductase inhibitors as antibacterial agents. *Biochem. Pharmacol. 71*, 941–948.
2. Pikis, A., Donkersloot, J. A., Rodriguez, W. J., and Keith, J. M. (1998) A conservative amino acid mutation in the chromosome-encoded dihydrofolate reductase confers trimethoprim resistance in *Streptococcus pneumoniae*. *J. Infect. Dis. 178*, 700–706.
3. Zhanel, G. G., Wang, X., Nichol, K., Nikulin, A., Wierzbowski, A. K., Mulvey, M., and Hoban, D. J. (2006) Molecular characterisation of Canadian paediatric multidrug-resistant *Streptococcus pneumoniae* from 1998−2004. *Int. J. Antimicrob. Agents 28*, 465–471.
4. Laue, H., Weiss, L., Bernardi, A., Hawser, S., Lociuro, S., and Islam, K. (2007) In vitro activity of the novel diaminopyrimidine, iclaprim, in combination with folate inhibitors and other antimicrobials with different mechanisms of action. *J. Antimicrob. Chemother. 60*, 1391–1394.
5. Frey, K. M., Liu, J., Lombardo, M. N., Bolstad, D. B., Wright, D. L., and Anderson, A. C. (2009) Crystal structures of wild-type and mutant methicillin-resistant *Staphylococcus aureus* dihydrofolate reductase reveal an alternate conformation of NADPH that may be linked to trimethoprim resistance. *J. Mol. Biol. 387*, 1298–1308.
6. Kohlhoff, S. A., and Sharma, R. (2007) Iclaprim. *Expert Opin. Invest. Drugs 16*, 1441–1448.
7. Periti, P. (1995) Brodimoprim, a new bacterial dihydrofolate reductase inhibitor: A minireview. *J. Chemother. 7*, 221–223.
8. Oefner, C., Bandera, M., Haldimann, A., Laue, H., Schulz, H., Mukhija, S., Parisi, S., Weiss, L., Lociuro, S., and Dale, G. E. (2009) Increased hydrophobic interactions of iclaprim with *Staphylococcus aureus* dihydrofolate reductase are responsible for the increase in affinity and antibacterial activity. *J. Antimicrob. Chemother. 63*, 687–698.
9. Volpato, J. P., and Pelletier, J. N. (2009) Mutational ‘hot-spots’ in mammalian, bacterial and protozoal dihydrofolate reductases associated with antifolate resistance: Sequence and structural comparison. *Drug Resist. Updates 12*, 28–41.
10. Adrian, P. V., and Klugman, K. P. (1997) Mutations in the dihydrofolate reductase gene of trimethoprim-resistant isolates of *Streptococcus pneumoniae*. *Antimicrob. Agents Chemother. 41*, 2406–2413.
11. Maskell, J. P., Sefton, A. M., and Hall, L. M. (2001) Multiple mutations modulate the function of dihydrofolate reductase in trimethoprim-resistant *Streptococcus pneumoniae*. *Antimicrob. Agents Chemother. 45*, 1104–1108.
12. Fierke, C. A., Johnson, K. A., and Benkovic, S. J. (1987) Construction and evaluation of the kinetic scheme associated with dihydrofolate reductase from *Escherichia coli*. *Biochemistry 26*, 4085–4092.
13. Datsenko, K. A., and Wanner, B. L. (2000) One-step inactivation of chromosomal genes in *Escherichia coli* K-12 using PCR products. *Proc. Natl. Acad. Sci. U.S.A. 97*, 6640–6645.
14. Roychowdhury-Saha, M., and Burke, D. H. (2006) Extraordinary rates of transition metal ion-mediated ribozyme catalysis. *RNA 12*, 1846–1852.
15. Murphy, D. J., and Benkovic, S. J. (1989) Hydrophobic interactions via mutants of *Escherichia coli* dihydrofolate reductase: Separation of binding and catalysis. *Biochemistry 28*, 3025–3031.

16. Jeong, S. S., and Gready, J. E. (1994) A method of preparation and purification of (4R)-deuterated-reduced nicotinamide adenine dinucleotide phosphate. *Anal. Biochem. 221*, 273–277.
17. Cody, V., Pace, J., Makin, J., Piraino, J., Queener, S. F., and Rosowsky, A. (2009) Correlations of Inhibitor Kinetics for *Pneumocystis jirovecii* and Human Dihydrofolate Reductase with Structural Data for Human Active Site Mutant Enzyme Complexes. *Biochemistry 48*, 1702–1711.
18. Lakowicz, J. R. (2006) Principles of fluorescence spectroscopy, 3rd ed., Springer, New York.
19. McCoy, A. J., Grosse-Kunstleve, R. W., Adams, P. D., Winn, M. D., Storoni, L. C., and Read, R. J. (2007) Phaser crystallographic software. *J. Appl. Crystallogr. 40*, 658–674.
20. Kim, H. S., Damo, S. M., Lee, S. Y., Wemmer, D., and Klinman, J. P. (2005) Structure and hydride transfer mechanism of a moderate thermophilic dihydrofolate reductase from *Bacillus stearothermophilus* and comparison to its mesophilic and hyperthermophilic homologues. *Biochemistry 44*, 11428–11439.
21. Zwart, P. H., Afonine, P. V., Grosse-Kunstleve, R. W., Hung, L. W., Ioerger, T. R., McCoy, A. J., McKee, E., Moriarty, N. W., Read, R. J., Sacchettini, J. C., Sauter, N. K., Storoni, L. C., Terwilliger, T. C., and Adams, P. D. (2008) Automated structure solution with the PHENIX suite. *Methods Mol. Biol. 426*, 419–435.
22. Emsley, P., and Cowtan, K. (2004) Coot: Model-building tools for molecular graphics. *Acta Crystallogr. D60*, 2126–2132.
23. Brunger, A. T., Adams, P. D., Clore, G. M., DeLano, W. L., Gros, P., Grosse-Kunstleve, R. W., Jiang, J. S., Kuszewski, J., Nilges, M., Pannu, N. S., Read, R. J., Rice, L. M., Simonson, T., and Warren, G. L. (1998) Crystallography & NMR system: A new software suite for macromolecular structure determination. *Acta Crystallogr. D54*, 905–921.
24. Brunger, A. T. (2007) Version 1.2 of the Crystallography and NMR system. *Nat. Protoc. 2*, 2728–2733.
25. Cameron, C. E., and Benkovic, S. J. (1997) Evidence for a functional role of the dynamics of glycine-121 of *Escherichia coli* dihydrofolate reductase obtained from kinetic analysis of a site-directed mutant. *Biochemistry 36*, 15792–15800.
26. Appleman, J. R., Howell, E. E., Kraut, J., and Blakley, R. L. (1990) Role of aspartate 27 of dihydrofolate reductase from *Escherichia coli* in interconversion of active and inactive enzyme conformers and binding of NADPH. *J. Biol. Chem. 265*, 5579–5584.
27. Kuzmic, P. (1996) Program DYNAFIT for the analysis of enzyme kinetic data: Application to HIV proteinase. *Anal. Biochem. 237*, 260–273.
28. Dann, J. G., Ostler, G., Bjur, R. A., King, R. W., Scudder, P., Turner, P. C., Roberts, G. C., and Burgen, A. S. (1976) Large-scale purification and characterization of dihydrofolate reductase from a methotrexate-resistant strain of *Lactobacillus casei*. *Biochem. J. 157*, 559–571.
29. Howell, E. E., Villafranca, J. E., Warren, M. S., Oatley, S. J., and Kraut, J. (1986) Functional role of aspartic acid-27 in dihydrofolate reductase revealed by mutagenesis. *Science 231*, 1123–1128.
30. Andrews, J., Fierke, C. A., Birdsall, B., Ostler, G., Feeney, J., Roberts, G. C., and Benkovic, S. J. (1989) A kinetic study of wild-type and mutant dihydrofolate reductases from *Lactobacillus casei*. *Biochemistry 28*, 5743–5750.
31. Appleman, J. R., Beard, W. A., Delcamp, T. J., Prendergast, N. J., Freisheim, J. H., and Blakley, R. L. (1990) Unusual transient- and steady-state kinetic behavior is predicted by the kinetic scheme operational for recombinant human dihydrofolate reductase. *J. Biol. Chem. 265*, 2740–2748.
32. Sawaya, M. R., and Kraut, J. (1997) Loop and subdomain movements in the mechanism of *Escherichia coli* dihydrofolate reductase: Crystallographic evidence. *Biochemistry 36*, 586–603.
33. Cody, V., Luft, J. R., and Pangborn, W. (2005) Understanding the role of Leu22 variants in methotrexate resistance: Comparison of wild-type and Leu22Arg variant mouse and human dihydrofolate reductase ternary crystal complexes with methotrexate and NADPH. *Acta Crystallogr. D61*, 147–155.
34. Li, R., Sirawaraporn, R., Chitnumsub, P., Sirawaraporn, W., Wooden, J., Athappilly, F., Turley, S., and Hol, W. G. (2000) Three-dimensional structure of *M. tuberculosis* dihydrofolate reductase reveals opportunities for the design of novel tuberculosis drugs. *J. Mol. Biol. 295*, 307–323.